Science Bulletin 71 (2026) 1064–1072

Contents lists available at ScienceDirect

Science Bulletin

journal homepage: www.elsevier.com/locate/scib

Article

Multi-resonance emitters with phosphorus-bridged cyclization: spectral narrowing synergized with accelerated reverse intersystem crossing

Tianjiao Fan [a,1], Qiwei Liu [b,1], Chunlin Xu [a], Xuewen Wang [c,d], Lei Wang [c], Zhigang Shuai [a,e], Dongdong Zhang [a,*], Lian Duan [a,b,*]

[a] Key Lab of Organic Optoelectronics and Molecular Engineering of Ministry of Education, Department of Chemistry, Tsinghua University, Beijing 100084, China
[b] Laboratory of Flexible Electronics Technology, Tsinghua University, Beijing 100084, China
[c] Wuhan National Laboratory for Optoelectronics, Huazhong University of Science and Technology, Wuhan 430000, China
[d] Foshan Xianhu Laboratory of the Advanced Energy Science and Technology Guangdong Laboratory, Foshan 528216, China
[e] School of Science and Engineering, The Chinese University of Hong Kong, Shenzhen 518172, China

ARTICLE INFO

Article history:
Received 30 August 2025
Received in revised form 10 December 2025
Accepted 31 December 2025
Available online 13 January 2026

Keywords:
Organic light emitting diode
Multi-resonance
Narrow emission
Heavy-atom effect
Spin-orbit coupling

ABSTRACT

While intramolecular cyclization effectively modulates photoelectronic properties of multi-resonance (MR)-thermally activated delayed fluorescence (TADF) emitters, simultaneous narrowing full width at half maxima (FWHM) of spectra and accelerating reverse intersystem crossing (RISC) remain a formidable challenge. Here, we introduce a phosphorus-carbon-bridged cyclization in MR skeletons to synergistically suppress high-frequency molecular vibrations via skeleton rigidification and enhance spin-orbital coupling through introducing heavy-atom effects. Implementing this approach, two blue emitters, phenylphosphine oxide-bridged (BCzBN-PO) and phenylphosphine sulfide-bridged (BCzBN-PS), are developed and exhibit emission peaks at 467 and 474 nm with FWHMs of 19 and 18 nm, respectively. Moreover, benefiting from the additional heavy atom effect of sulfur complementing that of phosphorus, BCzBN-PS achieved a kRISC of 8.5×10^5 s^{-1}, nearly 8-fold higher than that of BCzBN-PO (1.1×10^5 s^{-1}). In the non-sensitized device architecture, both emitters exhibited narrowband emission with a FWHM < 30 nm and a maximum external quantum efficiency (EQE) > 20%. Notably, BCzBN-PS, leveraging its higher upconversion rate, demonstrated a superior maximum EQE and lower efficiency roll-off. Furthermore, in the TADF-sensitized device configuration, the organic light-emitting diodes further validated the enhanced upconversion efficiency—evidenced by BCzBN-PS delivering a higher maximum EQE than BCzBN-PO (43.0% vs. 41.2%) and a reduced efficiency roll-off (30.1% vs. 25.9% at 1000 cd m^{-2}). This work establishes a molecular engineering paradigm that balances color purity and exciton utilization efficiency, paving new avenues for high-performance narrowband electroluminescence.

1. Introduction

Polycyclic aromatic hydrocarbons (PAHs) embedded with strategically para-positioned heteroatoms with opposing electronegativity, usually electron-rich nitrogen and electron-deficient boron atoms, would induce a multiple-resonance (MR) effect, which induces alternating localization of frontier molecular orbitals (FMOs) on single atoms [1–5]. This unique electronic configuration creates a short-range charge transfer (SRCT) transition, enabling not only narrowband emission with exceptional color purity but also relatively small singlet–triplet energy gap (ΔE_{ST}) for thermally activated delayed fluorescence (TADF) [6–9]. However, MR-TADF emitters exhibit relatively low reverse intersystem crossing rates (k_{RISC}) in the range of 10^3–10^4 s^{-1}, leading to pronounced efficiency roll-off in organic light-emitting diodes (OLEDs) compared to conventional TADF systems with twisted donor–acceptor (D-A) architectures [10–12]. Although D-A-type TADF or phosphorescent sensitizers can partially mitigate triplet accumulation in MR-TADF devices, enhancing intrinsic k_{RISC} remains critical for better electroluminescence at high brightness [13–16]. Therefore, strategies that could simultaneously narrow spectra and enhance RISC remain ongoing pursuit.

* Corresponding authors.
E-mail addresses: ddzhang@mail.tsinghua.edu.cn (D. Zhang), duanl@mail.tsinghua.edu.cn (L. Duan).
[1] These authors contributed equally to this work.

https://doi.org/10.1016/j.scib.2026.01.021
2095-9273/

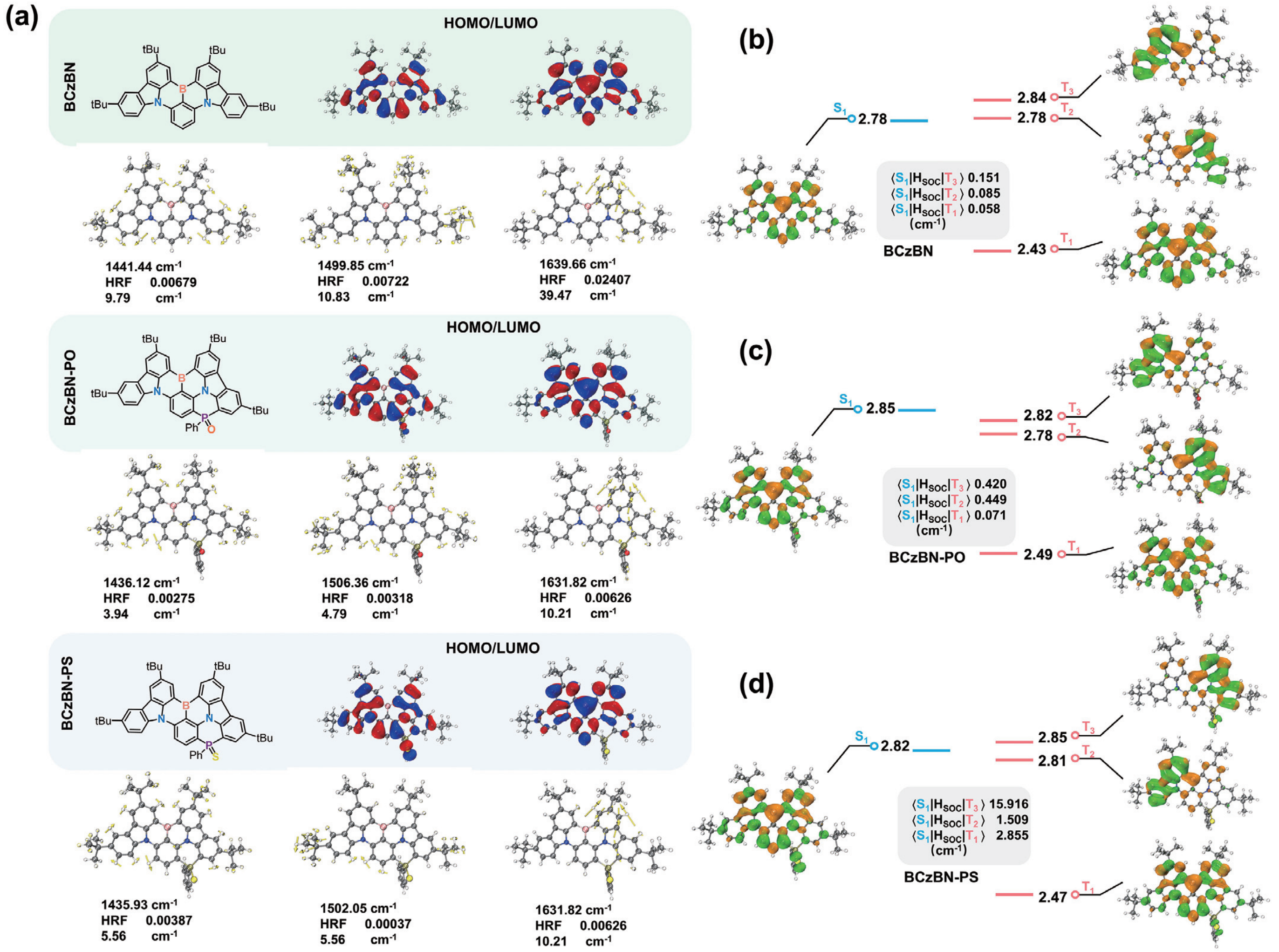

Fig. 2. Theoretical computation results. (a) HOMO/LUMO distributions, and selected vibrational modes of BCzBN, BCzBN-PO, and BCzBN-PS emitters obtained by B3LYP/6-311G(d,p) calculations. Simulated single-point energy diagrams, hole-charge distributions, and related norms of spin–orbit coupling matrix for (b) BCzBN, (c) BCzBN-PO, and (d) BCzBN-PS at the B3LYP/6-311G(d,p) level.

donating ability of the para-positioned carbazole fragment, therefore blue-shifting the emission band. Besides, stronger n*-π* hyperconjugation could be observed between the lone pair electrons of the oxygen/sulfur atom and the two nearby C–P bridge bonds' antibonding orbitals shown in Figs. S15c and S16c (online). And the second-order perturbation energy values are 14.57 kcal mol^{-1} for O (lone pair electrons) →C_{11}–P bond and could be up to 14.47 kcal mol^{-1} for O (lone pair electrons) →C_{33}–P bond. Though the values for BCzBN-PS tend to be lower, the second-order perturbation energy values remain to be 10.69 kcal mol^{-1} for S (lone pair electrons) →C_{11}–P bond and 9.71 kcal mol^{-1} for S (lone pair electrons) →C_{33}–P bond.

Moreover, the energies of the S_1 excited states were theoretically predicted to be 2.78 eV for BCzBN, 2.85 eV for BCzBN-PO and 2.82 eV for BCzBN-PS, respectively. Those results validate the hypothesis that the P(V)–C bridge ought to provide blue-shifted emission compared to BCzBN, while (phenyl)phosphine oxide bridge tends to promote the blue shift to a greater extent. As depicted in Fig. S17 (online), slightly smaller reorganization energy (λ) of merely 0.11 eV for both BCzBN-PO and BCzBN-PS compared to that of BCzBN (0.12 eV) could be observed. To further get a grip on the advantage that phosphorus cycle introduced on the emission band width for BCzBN-PO and BCzBN-PS over BCzBN, three major vibrational modes at relatively high vibration frequencies (approximately 1450, 1510, and 1650 cm^{-1}, respectively) of all three emitters were analyzed in detail as shown in Fig. 2a [35]. The vibration modes at approximately 1440 and 1500 cm^{-1} were both mainly related to the quasi-symmetrical in-plane C–C scissoring/rocking vibrations of the N-B-N bonded central phenyl ring, while the mode at approximately 1640 cm^{-1} was mainly related to asymmetrical in-plane C–C scissoring of the peripheral carbazole substituent at one side of the molecule. Obviously, no matter whether the phosphorus bridge contains oxygen or sulfur, the introduction of phosphorus bridge could suppress molecular vibration and contribute to smaller HR factors and reorganization energies in all vibrational modes to varying degrees, especially for the vibration mode at approximately 1650 cm^{-1} since such mode is strongly related to the peripheral carbazole substituent to which the phosphorus bridge would attach. Such a result suggests that compared to the primary MR planar structure BCzBN, the introduction of the phosphorus bridge could facilitate the suppression of the vibrations related to the central phenyl ring as well as the peripheral carbazole substituent that the phosphorus bridge bonded with, leading to a narrower emission spectrum.

Furthermore, to assess the effect of the phosphorus bridge on the RISC process, the single-point energy calculation based on the ground state S_0 and excited states S_1 and T_1 conformation of BCzBN, BCzBN-PO, and BCzBN-PS was also conducted as listed in Table S1 (online). As illustrated in Fig. 2b–d, the values of singlet–triplet energy gap (ΔE_{ST}) of all three emitters are calculated to be close to each other and at around the value of 0.35 eV. The hole-electron distributions and NTO analysis pointed out that the hole-charge character for these emitters is similar to each other under the same excited states among S_1 and T_1–T_3 states, since the SRCT-dominated character could be all found at S_1 and T_1 for all three emitters while the T_2 and T_3 states for BCzBN, BCzBN-PO, and BCzBN-PS exhibited more LRCT tendency [31,36]. The non-adiabatic coupling matrixes between triplet states of all three MR-TADF materials were also calculated at the level of UB3LYP/6-311G** using the Qchem 5.3 package in Fig. S18 (online), revealing that the Euclidean norms of each matrix are all over 1.0 between each triplet states, suggesting the strong coupling interactions between their triplet states. However, according to the simulation of SOC matrix elements (H_{SOC}) between S_1 and T_1 of those three emitters using ORCA package, the norm of the SOC matrix elements between S_1 and T_1 states ($\langle S_1|H_{SOC}|T_1\rangle$) for BCzBN is calculated to be 0.058 cm^{-1}; while the value for BCzBN-PO is 0.071 cm^{-1}, which could be attributed to a slight of the heavy atom effect introduced by the phosphorus atom of the phosphorus bridge, since phosphorus like sulfur is an element in the third period [37]. And such a heavy atom effect could be further enhanced by the sulfur atom, as the $\langle S_1|H_{SOC}|T_1\rangle$ value of BCzBN-PS could be as high as 2.86 cm^{-1}. Considering that the upconversion process of T_1 to S_1 might be accelerated by high-lying triplet states served as a mediating channel, the norms of the SOC matrix elements between S_1 and T_2–T_3 states for all three emitters have been also calculated [38,39]. For each emitter alone, $\langle S_1|H_{SOC}|T_2\rangle$ and $\langle S_1|H_{SOC}|T_3\rangle$ tend to be much larger than $\langle S_1|H_{SOC}|T_1\rangle$, which should be due to the enhanced LRCT character. And the norm values alone of the same matrix for each emitter all increase from BCzBN, BCzBN-PO to BCzBN-PS, which could also be attributed to the improvement of HAE like $\langle S_1|H_{SOC}|T_1\rangle$ matrix. Therefore, compared with BCzBN, though the phosphorus bridge could not help to decrease the ΔE_{ST}, the enlarged SOC between S_1 and triplet states could potentially accelerate the RISC process owing to the HAE introduced by phosphorus for BCzBN-PO and phosphorus with sulfur for BCzBN-PS.

3.3. Photophysical properties

The UV/vis absorption, fluorescence, and phosphorescence (under 77 K) spectra of BCzBN-PO, BCzBN-PS, and BCzBN in dilute toluene (1×10^{-5} mol L^{-1}) were measured as shown in Fig. 3a, b and Table 1. The absorption spectrum peaking at 456 and 462 nm of BCzBN-PO and BCzBN-PS were observed respectively. The fluorescence spectra of the emitters exhibited sharp blue emission bands peaking at 467 and 474 nm, with relatively small Stokes shifts of 11 and 12 nm for BCzBN-PO and BCzBN-PS, respectively, both of which showed blue shifted emission compared with BCzBN, resulting from the introduction of electron withdrawing P (V) fragments at the meta-position of the boron atom in the MR central phenyl ring. Additionally, impressive small FWHMs of 0.11 eV (19 nm) for BCzBN-PO and 0.10 eV (18 nm) for BCzBN-PS were also observed, both of which exhibited slightly narrower emission band compared with the parent molecule BCzBN for their stronger molecular rigidity brought by the (phenyl)phosphine oxide/(phenyl)phosphine sulfide bridge by phosphorus cyclization reaction, which also accorded well with the vibration analysis. The solvatochromic effect experiments of both emitters have been performed as shown in Fig. S20 (online), BCzBN-PO displayed an emission of small redshift of 7 nm varying the solvents from low-polarity cyclohexane (460 nm) to high-polarity dichloromethane (467 nm), as well as a redshift of 8 nm from cyclohexane (466 nm) to dichloromethane (474 nm) for BCzBN-PS, corresponding well with their SRCT character.

Calculated from the onset of the fluorescence and phosphorescence spectra, the S_1 and T_1 energy levels were estimated to be 2.72 and 2.61 eV for BCzBN-PO, while also estimated to be 2.67 and 2.55 eV for BCzBN-PS, respectively, from which the ΔE_{ST} of 0.11 eV for BCzBN-PO and 0.12 eV for BCzBN-PS could also be derived. As shown in Fig. 3c, the transient photophysical measurement offered short prompt lifetimes of 4.8 and 1.4 ns for BCzBN-PO and BCzBN-PS, respectively. Impressively, both emitters showed pronounced short lifetimes for the delayed part, which were measured to be 35 μs for BCzBN-PO and an even smaller value of 15 μs for BCzBN-PS. To further evaluate the materials as TADF emitters, the photoluminescence quantum yields (PLQYs) of BCzBN-PO and BCzBN-PS were measured under continuous nitrogen bubbling for 10 min, which turned out to high values of 99% and 98%, respectively.

Additionally, under air atmosphere, the PLQYs measured in toluene reduced to as low as 26% and 8% for BCzBN-PO and BCzBN-PS, respectively, manifesting relatively high ratios of delayed parts of 73% and 90% for the two emitters, which were supported by the greatly enhanced SOC calculated for both molecules. Based on these measurements, rather fast radiative decay rates (k_r) of 2.1×10^8 and 7.1×10^8 s^{-1} were obtained for BCzBN-PO and BCzBN-PS, respectively, as well as high RISC rates (k_{RISC}) of 1.1×10^5 s^{-1} for BCzBN-PO and 8.5×10^5 s^{-1} for BCzBN-PS, which stand for nearly two orders of magnitude higher than ordinary multi-resonance emitters, corresponding well with the enhanced SOC values. Photophysical properties of BCzBN-PO, BCzBN-PS, and BCzBN were also measured in the film of 2,8-bis (diphenylphosphoryl)-dibenzo[b,d]furan (PPF) with 2 wt% doping concentration, as shown in Table S2 and Fig. S21 (online), exhibited red-shifted emissions with slightly broadened FWHMs, as well as similar k_{RISC}s of 1.0×10^5 and 7.1×10^5 s^{-1} for BCzBN-PO and BCzBN-PS, respectively, corresponding well to that derived from measurement in toluene solution.

Moreover, compared with previously reported analogous MR-TADF emitters modified with locked bridges at the meta-position of the boron atom to enhance structure rigidity thus suppress distortion and vibrational couplings of excited states, aiming to acquire narrower emission bands and superior performances in OLED devices, BCzBN-PO and BCzBN-PS exhibited distinct strengths both on FWHMs and the RISC process. Among the representative MR-TADF molecules, which adopt intramolecular cyclization strategies to anchor the external phenyl groups of MR fragments, displayed in Fig. 3d, BCzBN-PS predominates with the highest rates of RISC over all emitters, even surpassing the double-sulfur locking MR-TADF emitter reported by Wang and co-workers [21], which embedded two sulfur atoms directly at the meta-site of boron, possessing a high RISC rate of 10^5 s^{-1} magnitude brought by the strong heavy-atom effect. At the same time, BCzBN-PO and BCzBN-PS show remarkably small FWHMs of 0.11 and 0.10 eV, indicating better performances on narrowing emission bands than the majority of emitters harnessing the interlocking design, demonstrating the effectiveness of our innovative strategy of adopting P=S and P=O fragments as the locking bridge to suppress emission broadening while simultaneously accelerating RISC process through heavy-atom effect to elevate the utilization efficiency of triplet exciton under electrical excitation, thus showing great potential of both high color purity and highly efficient emitters for OLED devices.

3.4. Device fabrication and characterization

To further investigate the performances of BCzBN-PO and BCzBN-PS as emitters in OLEDs, the devices were fabricated with the structure of indium tin oxide (ITO)/1,4,5,8,9,11-hexaazatriphe nylene hexacarbonitrile (HATCN) (5 nm)/4,4′-cyclohexylidenebis[

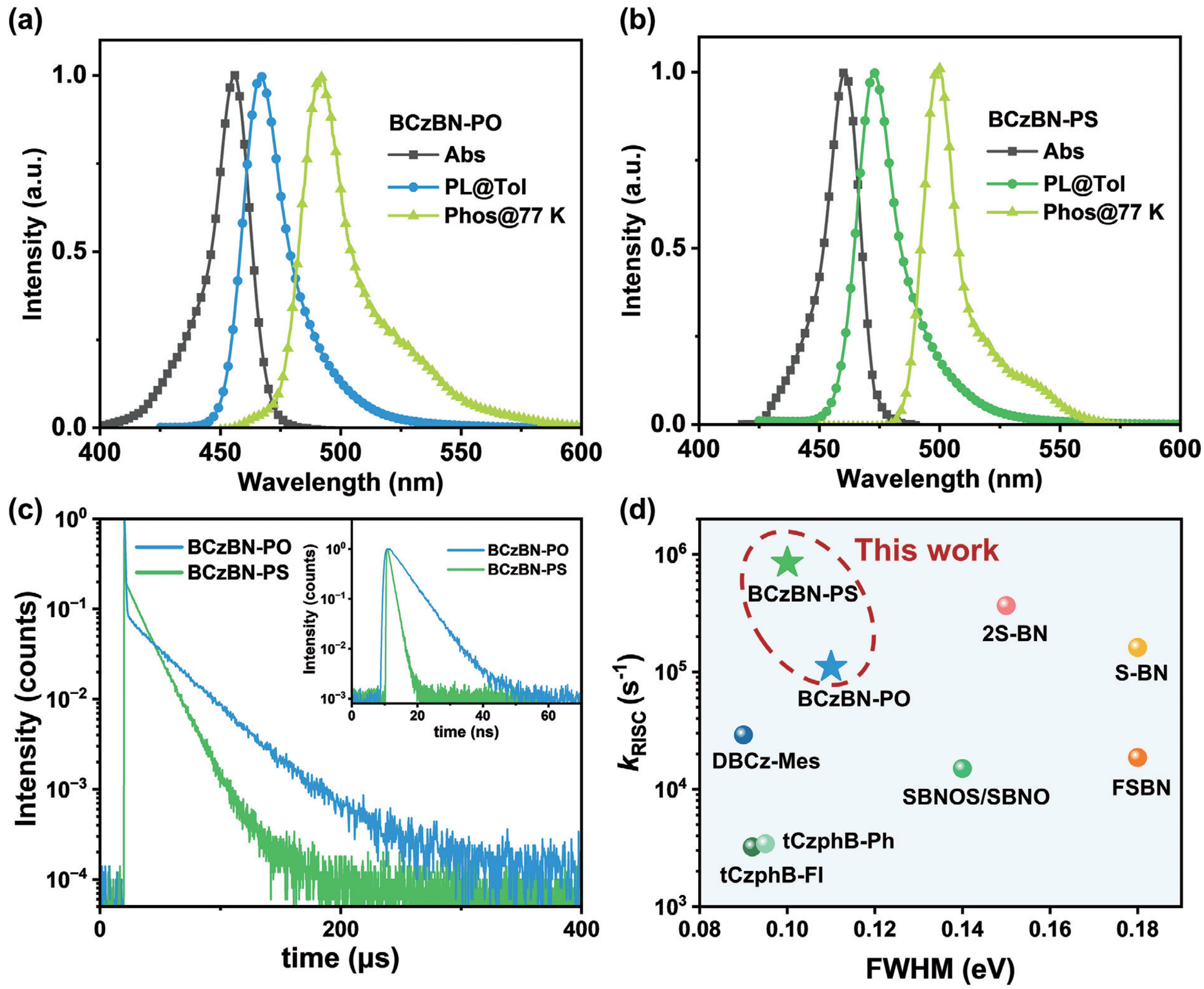

Fig. 3. Photophysical properties of BCzBN-PO and BCzBN-PS. Normalized UV–vis absorption, fluorescence, and phosphorescence (under 77 K) spectra of (a) BCzBN-PO and (b) BCzBN-PS in toluene. (c) Transient photoluminescence decay curves of BCzBN-PO and BCzBN-PS in dilute toluene after N_2-bubbling for 15 min. (d) Representative MR-TADF molecules adopting interlocking strategies for spectra narrowing and upconversion acceleration.

Table 1
Summary of the photophysical properties of BCzBN-PO, BCzBN-PS, and BCzBN.

Compound	λ_{abs} [a] (nm)	λ_{em} [a] (nm)	FWHM (nm/eV)	E_{S_1} [b] (eV)	E_{T_1} [b] (eV)	ΔE_{ST} [b] (eV)	ϕ_{PL} [c] (%)	τ_p(ns)	τ_d(μs)	k_r [d] (10^8 s^{-1})	k_{RISC} [d] (10^5 s^{-1})
BCzBN-PO	456	467	19/0.11	2.72	2.61	0.11	99	4.8	35	2.1	1.1
BCzBN-PS	461	474	18/0.10	2.67	2.55	0.12	98	1.4	15	7.1	8.5
BCzBN	468	483	24/0.13	2.66	2.53	0.13	89	6.0	81	1.7	0.14

[a] Measured in toluene (1×10^{-5} mol L^{-1}) at 298 K.
[b] Estimated from the onset of the spectra. $\Delta E_{ST} = E_{S_1} - E_{T_1}$.
[c] Measured in a photometric integrating sphere in nitrogen-bubbling toluene.
[d] Estimated based on the data obtained in dilute toluene solution.

N,N-bis(p-tolyl)aniline] (TAPC) (30 nm)/tris(4-(9H-carbazol-9-yl) phenyl)amine (TCTA) (10 nm)/3-bis(9H-carbazol-9-yl)benzene (mCP) (5 nm)/the emitting layer (EML, 24 nm)/2,8-bis (diphenylphosphoryl)-dibenzo[b,d]furan (PPF) (5 nm)/4,7-diphenyl-1,10-phenanthroline (Bphen) (30 nm)/LiF (0.5 nm)/Al (150 nm). The device architecture with energy levels and molecular structures of materials possibly used during the device fabrication was illustrated in Fig. 4a. As illustrated in Fig. S24 (online), a non-sensitized binary system EML was firstly used and investigated, in which PPF was used as the host while BCzBN-PO/ BCzBN-PS were used as dopants with the doping concentration of 2 wt%. Both emitters showed narrowband emission with FWHMs < 30 nm with maximum EQEs > 20%, while BCzBN-PS-based device showed a lower efficiency roll-off compared with that of BCzBN-PO, which could attribute to the more accelerated upconversion capacity of BCzBN-PS. However, the corresponding electroluminescence devices with binary EMLs generally still suffered from low maximum luminance as well as relatively large efficiency roll-offs, which was possibly because that the k_{RISC} rates for BCzBN-PO and BCzBN-PS are still lower than that of conventional TADF materials, and the doping concentration was insufficient for harvesting triplets between dopant-dopant via Dexter transfer mechanism (DET) on which triplet exciton transportation mainly relies, since the distance between two dopant molecules has been pro-

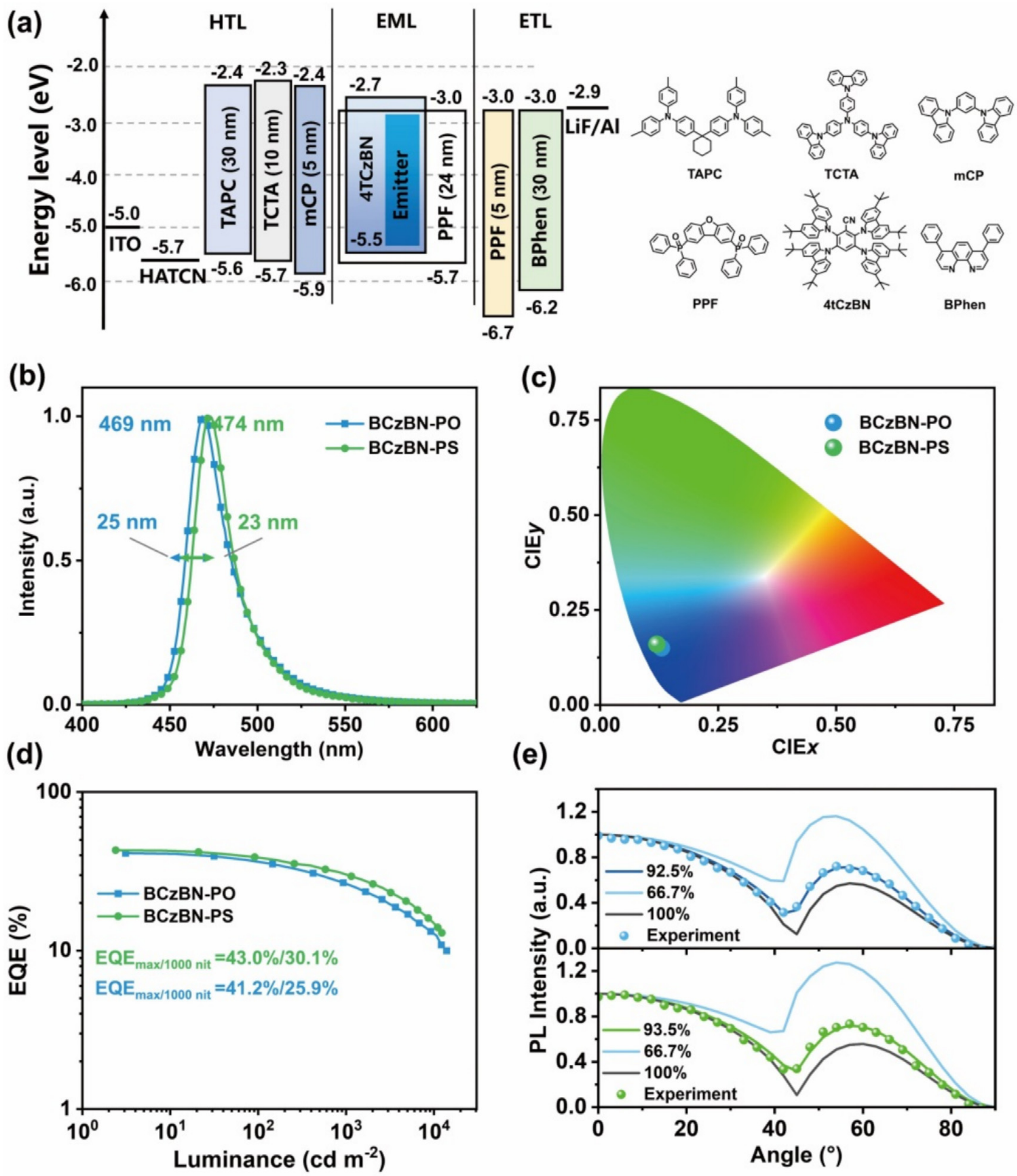

Fig. 4. Device performances of OLEDs based on BCzBN-PO and BCzBN-PS. (a) Energy level diagram of the device and molecules used in the fabrication of OLEDs, (b) normalized EL spectra and device in operation under 1000 cd m^{-2}, (c) CIE coordinates of the OLEDs, (d) EQE versus luminance curves of 2 wt% BCzBN-PO/BCzBN-PS devices, and (e) angle-dependent p-polarized PL intensity and simulation curve for BCzBN-PO/BCzBN-PS in PPF film with 2 wt% doping concentration.

longed due to low doping concentration in EML [40]. Since it is a dilemma that a low doping concentration is not conducive to the efficiency and roll-off of OLED devices while a high doping concentration is likely to lead to concentration aggregation quenching as well as spectral broadening, a TADF sensitizer is usually adopted to the EML to balance charge transport, promote energy transfer as well as assist the recycling of triplet excitons under electrical excitation [6]. Therefore, a TADF sensitizer, 4tCzBN, was adopted to construct the TADF-sensitized devices with optimal doping concentrations of 30 wt% and 2 wt% for the sensitizer and emitters, respectively [41]. Significant spectrum overlap between the absorption of BCzBN-PO/BCzBN-PS and the emission of 4tCzBN was observed shown in Fig. S25 (online) and the radius (R_0) of Förster energy transfer (FRET) were calculated to be 42.6 and 42.5 Å for BCzBN-PO and BCzBN-PS, individually. The device performances of both sensitized and non-sensitized OLEDs based on BCzBN-PO and BCzBN-PS were summarized in Table 2. The EL spectrum of the sensitized devices recorded at 1000 cd m^{-2} is shown in Fig. 4b, c, exhibiting pure blue emission peaking at 469 nm with a FWHM of 25 nm for BCzBN-PO, as well as 474 nm with a FWHM of 23 nm for BCzBN-PS, of which the CIE coordinates of (0.13, 0.15) and (0.12, 0.16) are obtained individually. The EL spectra of both emitters were slightly broadened as most MR-TADF emitters reported before, which could be probably attributed to the interactions between the host material and the emitters. And the EQE-luminance details of devices exhibited in Fig. 4d revealed remarkably ultrahigh maximum EQEs of 41.2% and 43.0% for BCzBN-PO and BCzBN-PS, respectively, which hold the cutting edge of contemporary blue OLED devices adopting MR-TADF molecules. Besides, BCzBN-PS-based device still obtained

Table 2
Summary of the EL data of BCzBN-PO and BCzBN-PS based devices.

Device	λ_{em} [a] (nm)	FWHM[a] (nm)	CE_{max} (cd A^{-1})	PE_{max} (lm W^{-1})	V_{on} [b] (V)	EQE[c] (%)	CIE[a](x, y)
Sensitized-BCzBN-PO	469	25	46.5	40.2	3.5	41.2/24.9	(0.13, 0.15)
Sensitized-BCzBN-PS	473	23	51.5	45.6	3.5	43.0/30.1	(0.12, 0.16)
Non-sensitized-BCzBN-PO	472	29	15.5	10.8	5.2	21.7/2.3	(0.14, 0.17)
Non-sensitized-BCzBN-PS	474	24	26.7	26.2	6.1	22.4/7.1	(0.11, 0.17)

[a] Values recorded at the luminance of 1000 cd m^{-2}.
[b] Turn-on voltage of the devices at 1 cd m^{-2}.
[c] Maximum external quantum efficiencies and values at 1000 cd m^{-2}, respectively.

a lower efficiency roll-off with an EQE of 30.1% at 1000 cd m^{-2}, compared with that of BCzBN-PO with a relatively lower EQE of 25.9% at the same operational luminance. As shown in Fig. S27 (online), unlike non-sensitized binary EML in which emitters have to harvest triplets mainly by themselves, the TADF sensitizer could harvest excitons via accelerated upconversion capacity and transfer them to emitter molecules through Förster transfer mechanism (FRET). Though most singlet excitons could be transferred to both emitters from TADF sensitizer and host by means of FRET, a portion of triplet excitons may be generated at the triplet state at the TADF sensitizer as well as at the MR-TADF emitter itself due to their likewise intrinsic intersystem crossing, which could be possibly accumulated at the T_1 state of the emitter itself. For non-sensitized device, since the intersystem conversion (ISC) process of emitters exists, a large amount of triplet excitons could accumulate under high operating lumiance. In addition, DET from the triplet of the TADF sensitizer to that of emitters could happen in TADF-sensitized device, also causing accumulation of the triplet states of emitters, leading to lowered exciton utilization efficiency and efficency roll-off, especially under high luminance. Therefore, an enhanced rate of upconversion of the emitter itself would facilitate a higher maximum EQE as well as a smaller efficiency roll-off at high operational luminance. As a result, compared with other rationally designed MR-TADF emitters adopting analogous locking bridge strategies listed in Table S4 (online) and Fig. 3d, BCzBN-PO and BCzBN-PS still dominate on device performances considering outstanding maximum EQEs over 40%, which are in agreement with the corresponding superior RISC rates over the magnitude of 10^5 s^{-1} [3,42].

To further explain the cause of high EQEs of the related device, the angle-dependent p-polarized photoluminescence spectra were analyzed for both emitters doped in PPF films with 2 wt% doping concentration [43–47]. As shown in Fig. 4e, horizontal emission dipole orientation ratios ($\Theta_{||}$) of 92.5% and 93.5% were obtained for BCzBN-PO and BCzBN-PS, respectively. The relatively high horizontal dipole orientation ratios could conduce to greater optical outcoupling efficiency compared with randomly oriented molecules, also explaining the superb device performances over maximum EQEs of 40%, which is in agreement with the device performance results above. Angle-dependent EL intensity of the devices was also measured as shown in the Figs. S28 and S29 (online). The angular-light distribution curves of both sensitized devices showed a basically Lambertian pattern, also confirming the validation of the high EQE values.

4. Conclusion

To sum up, to simultaneously narrow the emission band as well as promote the RISC rates, we have taken the lead in employing phosphorus locking bridges connecting the MR-TADF emitting core BCzBN's boron-meta position site with its peripheral phenyl ring. As it turned out, the phosphorus bridge could improve molecular framework rigidity, suppress the related irreversible geometry relaxation during excitation, and thereby narrow the major emission band. More importantly, the RISC rates are enhanced via the increased SOC due to the HAE triggered by phosphorus from the phosphorus bridge, which could be further improved once sulfur is introduced to the phosphorus bridge. As a result, BCzBN-PO exhibited a blue emission with a FWHM of 19 nm in dilute toluene solution and an accelerated k_{RISC} of 1.1×10^5 s^{-1}, while BCzBN-PS showed an even narrower emission with a FWHM of 18 nm in dilute toluene solution and a further improved k_{RISC} of 8.5×10^5 s^{-1}. The related BCzBN-PO-based OLED device could reach an impressive maximum EQE of 41.2%, and that for BCzBN-PS could be even as high as 43.0%, which is accompanied by mitigatory efficiency roll-off thanks to an enhanced RISC rate. As a result, our molecular design here is of great significance from the perspective of exploring higher color purity as well as improved device performance for narrowband MR-TADF emitters. Moreover, our work has confirmed the possibility of using this locking bridge method to improve the spectrum and enhance upconversion, shedding new light on further introducing more types of heteroatoms (such as silicon or selenium) through methods such as transition metal catalysis and nucleophilic substitution to construct similar structures and directionally modulate the photophysical properties of MR-TADF emitters.

Conflict of interest

The authors declare that they have no conflict of interest.

Acknowledgments

This work was supported by the National Natural Science Foundation of China (52222308 and 22135004), the National Key Research and Development Program (2023YFE0203300 and 2024YFB3612100), the Guangdong Basic and Applied Basic Research Foundation (2021B1515120041), the Open Project Program of Wuhan National Laboratory for Optoelectronics (2023WNLOKF010), and the National Natural Science Foundation of China's Youth Project for Doctoral Students (524B2035).

Author contributions

Tianjiao Fan and Qiwei Liu performed the molecular synthesis and chemical characterization, the photophysical measurements, and the device characterization. Chunlin Xu and Zhigang Shuai performed the theoretical calculation. Dongdong Zhang and Lian Duan devised the conceptual idea and supervised experiments. All authors contributed to writing the manuscript.

Appendix A. Supplementary material

Supplementary data to this article can be found online at https://doi.org/10.1016/j.scib.2026.01.021.

References

[1] Hatakeyama T, Shiren K, Nakajima K, et al. Ultrapure blue thermally activated delayed fluorescence molecules: efficient HOMO–LUMO separation by the multiple resonance effect. Adv Mater 2016;28:2777–81.
[2] Kondo Y, Yoshiura K, Kitera S, et al. Narrowband deep-blue organic light-emitting diode featuring an organoboron-based emitter. Nat Photonics 2019;13:678–82.
[3] Fan T, Du M, Jia X, et al. High-efficiency narrowband multi-resonance emitter fusing indolocarbazole donors for BT. 2020 red electroluminescence and ultralong operation lifetime. Adv Mater 2023;35:2301018.
[4] Sano Y, Shintani T, Hayakawa M, et al. One-shot construction of BN-embedded heptadecacene framework exhibiting ultra-narrowband green thermally activated delayed fluorescence. J Am Chem Soc 2023;145:11504–11.
[5] Yang M, Park IS, Yasuda T. Full-color, narrowband, and high-efficiency electroluminescence from boron and carbazole embedded polycyclic heteroaromatics. J Am Chem Soc 2020;142:19468–72.
[6] Fan X-C, Wang K, Shi Y-Z, et al. Ultrapure green organic light-emitting diodes based on highly distorted fused π-conjugated molecular design. Nat Photonics 2023;17:280–5.
[7] Zhang Y, Wei J, Zhang D, et al. Sterically wrapped multiple resonance fluorophors for suppression of concentration quenching and spectrum broadening. Angew Chem Int Ed 2022;61:e202113206.
[8] Fan T, Zhu S, Cao X, et al. Tailored design of π-extended multi-resonance organoboron using indolo[3,2-b]indole as a multi-nitrogen bridge. Angew Chem Int Ed 2023;62:e202313254.
[9] Zhang Y, Wei J, Wang L, et al. Multiple fusion strategy for high-performance yellow OLEDs with full width at half maximums down to 23 nm and external quantum efficiencies up to 37.4%. Adv Mater 2023;35:2209396.
[10] Madayanad Suresh S, Hall D, Beljonne D, et al. Multiresonant thermally activated delayed fluorescence emitters based on heteroatom-doped nanographenes: recent advances and prospects for organic light-emitting diodes. Adv Funct Mater 2020;30:1908677.
[11] Lee HL, Kang J, Lim J, et al. Hybridization of short-range and long-range charge transfer excited states in multiple resonance emitter. Nat Commun 2023;14:4818.
[12] Lee HL, Jeon SO, Kim I, et al. Multiple-resonance extension and spin-vibronic-coupling-based narrowband blue organic fluorescence emitters with over 30% quantum efficiency. Adv Mater 2022;34:2202464.
[13] Fan T, Liu Q, Zhang H, et al. Enhancing spin–orbit coupling in an indolocarbazole multiresonance emitter by a sulfur-containing peripheral substituent for a fast reverse intersystem crossing. Adv Mater 2024;36:2408816.
[14] Huang T, Wang Q, Meng G, et al. Accelerating radiative decay in blue through-space charge transfer emitters by minimizing the face-to-face donor–acceptor distances. Angew Chem Int Ed 2022;61:e202200059.
[15] Lei B, Huang Z, Li S, et al. Medium-ring strategy enables multiple resonance emitters with twisted geometry and fast spin-flip to suppress efficiency roll-off. Angew Chem Int Ed 2023;62:e202218405.
[16] Huang F, Cheng Y-C, Wu H, et al. Hanging heavy atom-containing chains onto a multiple resonance framework: influence on the TADF properties and device performances. Chem Eng J 2023;465:142900.
[17] Meng G, Zhou J, Wang Q, et al. Isomeric pentagonal fusion and π-expanding of nitrogen/carbonyl-containing multi-resonant emitters for high-performance and narrowband organic electroluminescence. Adv Funct Mater 2025;35:2422973.
[18] Meng G, Zhou J, Huang T, et al. B–N/B–O contained heterocycles as fusion locker in multi-resonance frameworks towards highly-efficient and stable ultra-narrowband emission. Angew Chem Int Ed 2023;62: e202309923.
[19] Wang X, Zhang Y, Dai H, et al. Mesityl-functionalized multi-resonance organoboron delayed fluorescent frameworks with wide-range color tunability for narrowband OLEDs. Angew Chem Int Ed 2022;61:e202206916.
[20] Wang Z, Li D, Li W, et al. Multiple charge transfer processes enable blue emitter for highly efficient OLEDs. Adv Opt Mater 2023;11:2300017.
[21] Pu Y, Jin Q, Zhang Y, et al. Sulfur-locked multiple resonance emitters for high performance orange-red/deep-red OLEDs. Nat Commun 2025;16:332.
[22] Pu Y, Cai X, Qu Y, et al. Spiro-carbon-locking and sulfur-embedding strategy for constructing deep-red organic electroluminescent emitter with high efficiency. Angew Chem Int Ed 2025;64:e202420253.
[23] Liu J, Zhu Y, Tsuboi T, et al. Toward a BT.2020 green emitter through a combined multiple resonance effect and multi-lock strategy. Nat Commun 2022;13:4876.
[24] Fan T, Zhang Y, Wang L, et al. One-shot synthesis of B/N-doped calix[4]arene exhibiting narrowband multiple resonance fluorescence. Angew Chem Int Ed 2022;61:e202213585.
[25] Huang T, Xu Y, Lu X, et al. Modulating charge-transfer excited states of multiple resonance emitters via intramolecular covalent bond locking. Angew Chem Int Ed 2024;63:e202411268.
[26] Li H-Z, Xie F-M, Bai J-Y, et al. Spiral-locking strategy for efficient narrowband multiple resonance thermally activated delayed fluorescence emitters. Small 2024;20:2407220.
[27] McNeill JN, Bard JP, Johnson DW, et al. Azaphosphinines and their derivatives. Chem Soc Rev 2023;52:8599–634.
[28] Vonnegut CL, Shonkwiler AM, Khalifa MM, et al. Facile synthesis and properties of 2-λ5-phosphaquinolines and 2-λ5-phosphaquinolin-2-ones. Angew Chem Int Ed 2015;54:13318–22.
[29] Murray JS, Politzer P. The electrostatic potential: an overview. Wires Comput Mol Sci 2011;1:153–63.
[30] Stephens PJ, Devlin FJ, Chabalowski CF, et al. Ab initio calculation of vibrational absorption and circular dichroism spectra using density functional force fields. J Phys Chem C 1994;98:11623–7.
[31] Lu T, Chen F. Multiwfn: a multifunctional wavefunction analyzer. J Comput Chem 2012;33:580–92.
[32] Lu T. A comprehensive electron wavefunction analysis toolbox for chemists. Multiwfn J Chem Phys 2024;161:082503.
[33] de Cózar A, Romero-Nieto C. Boundaries of the hyperconjugation from π-extended six-membered phosphorus heterocycles. Inorg Chem 2023;62:4097–105.
[34] Larrañaga O, Romero-Nieto C, de Cózar A. Dismantling the hyperconjugation of π-conjugated phosphorus heterocycles. Chem Eur J 2019;25:9035–44.
[35] Shuai Z. Thermal vibration correlation function formalism for molecular excited state decay rates. Chin J Chem 2020;38:1223–32.
[36] Liu Z, Lu T, Chen Q. An sp-hybridized all-carboatomic ring, cyclo[18]carbon: electronic structure, electronic spectrum, and optical nonlinearity. Carbon 2020;165:461–7.
[37] Neese F. The ORCA program system. Wires Comput Mol Sci 2012;2:73–8.
[38] Huang Z, Xie H, Miao J, et al. Charge transfer excited state promoted multiple resonance delayed fluorescence emitter for high-performance narrowband electroluminescence. J Am Chem Soc 2023;145:12550–60.
[39] Kang J, Lee HL, Jeon SO, et al. Spin-flip-restricted multiple-resonance emitters for extended device lifetime in indolocarbazole-based blue organic light-emitting diodes. Adv Sci 2024;11:2405604.
[40] Bolotin DS, Bokach NA, Demakova MY, et al. Metal-involving synthesis and reactions of oximes. Chem Rev 2017;117:13039–122.
[41] Zhang D, Cai M, Zhang Y, et al. Sterically shielded blue thermally activated delayed fluorescence emitters with improved efficiency and stability. Mater Horiz 2016;3:145–51.
[42] Yin C, Zhang Y, Huang T, et al. Highly efficient and nearly roll-off–free electrofluorescent devices via multiple sensitizations. Sci Adv 2022;8: eabp9203.
[43] Hua T, Cao X, Miao J, et al. Deep-blue organic light-emitting diodes for ultrahigh-definition displays. Nat Photonics 2024;18:1161–9.
[44] Chen Y, Zhang D, Zhang Y, et al. Approaching nearly 40% external quantum efficiency in organic light emitting diodes utilizing a green thermally activated delayed fluorescence emitter with an extended linear donor–acceptor–donor structure. Adv Mater 2021;33:2103293.
[45] Patil VV, Lee HL, Kim I, et al. Purely spin-vibronic coupling assisted triplet to singlet up-conversion for real deep blue organic light-emitting diodes with over 20% efficiency and y color coordinate of 0.05. Adv Sci 2021;8:2101137.
[46] Kim S-Y, Jeong W-I, Mayr C, et al. Organic light-emitting diodes with 30% external quantum efficiency based on a horizontally oriented emitter. Adv Funct Mater 2013;23:3896–900.
[47] Tenopala-Carmona F, Lee OS, Crovini E, et al. Identification of the key parameters for horizontal transition dipole orientation in fluorescent and TADF organic light-emitting diodes. Adv Mater 2021;33:2100677.